2009 American Control Conference
Hyatt Regency Riverfront, St. Louis, MO, USA
June 10-12, 2009

Theory for image-based identification of SPM dynamics

G. M. Clayton and S. Devasia

Abstract— **Rather than use external sensors, images of standard calibration samples can be used to model and correct positioning errors, caused by dynamics effects, in scanning probe microscopes (SPMs). The main contribution of the current article is the development of conditions, on the calibration sample and the scan trajectory, that allow for the image-based identification of SPM-nanopositioner dynamics.**

I. INTRODUCTION

In this article, conditions are developed for the image-based identification of scanning probe microscope (SPM) nanopositioner dynamics. Knowledge of the nanopositioner dynamics can be used in feedback and feedforward control design to improve the positioning speed, which is needed for rapid imaging and manipulation of dynamic surface phenomena using SPMs, e.g., see recent survey [1]. Rather than use external sensors to measure the nanopositioner dynamics, recent works have proposed the use of images (of standard calibration samples) to model and correct positioning errors in SPMs [2]-[6]. The main contribution of the current article is the development of conditions that allow for the image-based identification of SPM-nanopositioner dynamics. In particular, we present requirements on (and relations between): (a) the minimum spacing between features and the orientation of the calibration sample, and (b) the amplitude and frequency content of the SPM-probe's position trajectory.

Image-based approaches to modeling and control of SPM nanopositioners are advantageous in three cases: (i) when, both, high (angstrom scale) resolution and high operating speed are needed; (ii) in highly parallel nanopositioning systems; and (iii) for sensor calibration. First, the resolution of conventional sensors is limited during wide-bandwidth (high-speed) operations. For example, while the theoretical resolution of non-contact capacitive sensors is only limited by quantum noise, the effective noise factor is around $0.02nm/\sqrt{Hz}$ at room temperature. Thus, the resolution at $1000Hz$ is about $2nm$, which precludes the measurement of angstrom-scale SPM motion. In contrast, image-based methods exploit the existing, high-resolution, vertical sensor (probe-sample interaction) to achieve high-resolution estimates of the lateral position. Second, even when angstrom-scale resolution is not necessary, position measurements may be unavailable due to sensor integration issues, especially in highly-parallel SPMs (with parallel SPM probes) being developed to increase the throughput of SPM-based nanotechnologies [7]-[10]. In such highly-parallel SPMs, image-based approaches can be automated to model the dynamics, thereby enabling improved control of each SPM probe. Third, even when sensors are available (such as embedded sensors for highly-parallel SPMs [1]), an image-based approach enables the independent calibration of the sensor dynamics to account for issues such as sensor misalignment, failure, and cross coupling [11]. Therefore, it is desirable to develop image-based methods to model and correct SPM-nanopositioning errors. Early work used distortions in SPM images of standard calibration samples to correct static (DC-gain and nonlinear) effects in SPM nanopositioners [2]-[4]. More recently, image distortions have been used to model and correct dynamic effects that cause vibrations in SPM nanopositioners [5], [6].

In this article, we identify properties of the calibration-sample and scan trajectory that are needed for image-based modeling of the SPM-nanopositioner dynamics. The main issue is to estimate the achieved position trajectory for a given input to the nanopositioner. Sampled data points (positions at different time instants) can be found using the acquired image as shown in [5], [6]; the position trajectory needs to be then reconstructed from the sampled data points. Difficulty arises because, (a) the number and (b) the time spacing between the sampled data points depend on both the properties of the calibration sample as well as the position trajectory – these, in turn, affect the ability to reconstruct the position trajectory. Hence, reconstruction theorems [12], [13] for non-uniformly-sampled signals are used, in this article, to develop conditions on the calibration sample for guaranteed reconstruction of the position trajectory with the image-based approach. The implications of these conditions, for modeling the dynamics of SPM nanopositioners, are discussed using a scanning tunneling microscope (STM) example.

G. M. Clayton is with the Department of Mechanical Engineering, Villanova University, 800 Lancaster Avenue, Villanova, PA, 19083 USA e-mail: garrett.clayton@villanova.edu.

S. Devasia is with the Department of Mechanical Engineering, University of Washington, Box 352600, Seattle, WA 98195 USA e-mail: sdevasia@u.washington.edu.

II. PROBLEM FORMULATION AND SOLUTION

A. SPM Imaging

To acquire an image, the SPM probe is scanned above a surface as depicted in Fig. 1(a). Typically, a square area (Fig. 1(a)) is scanned by using a periodic probe-position trajectory in the x direction and an increasing probe-position trajectory in the y direction, as shown in Fig. 1(b). During this scanning process, tip-surface interactions can be measured and plotted to create an image. For example, in the scanning tunneling microscope (STM), variations in the tunneling current between the probe-tip and sample surface (related to the distance between the sample and the probe-tip as well as the sample's electronic properties [14]) can

978-1-4244-4524-0/09/$25.00 ©2009 AACC

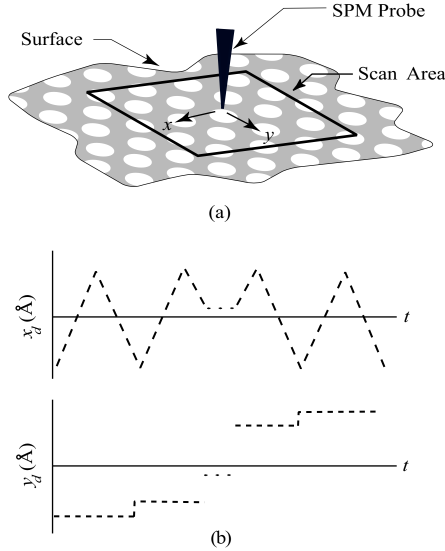

Fig. 1. Illustration of the SPM scan process. (a) The SPM probe scans an area over the calibration surface, following (b) the desired x_d and y_d trajectories (raster scan pattern).

be measured and plotted with respect to the desired probe position (x_d, y_d) to produce an image as shown in Fig. 2(a).

Positioning errors lead to distortions in images. For example, if there is substantial difference between the desired SPM-probe position (x_d, y_d) and actual position trajectories (x, y), then the resulting images (plotted using x_d, y_d) will be distorted as shown in Fig. 2(b). As discussed before, poor sensor resolution during wide-bandwidth (high-speed) SPM operation limits the ability to measure and therefore to plot the sensor data against the actual x and y positions to obtain an image. Moreover, even if sensor data was available, positioning errors $(x \neq x_d,\ y \neq y_d)$ will lead to undesirable distortions of the achieved nanoscale features in SPM-based nanofabrication applications. Therefore, there is a need to correct SPM positioning errors.

B. Image-based approach to modeling

1) Need to estimate position trajectory for modeling: Models of the SPM dynamics have been used to correct for positioning errors using feedback and feedforward control methods [1], [6], [15]. To obtain a model of the (linear or nonlinear) input-output relationship G,

$$G : u \rightarrow x \tag{1}$$

the probe position x needs to be known for different inputs u. If available, the input-output data can be used to identify the nanopositioner dynamics G using standard, model-identification techniques, e.g., linear SPM models are developed in [6] and nonlinear models are developed in [16]. However, the position x cannot be directly measured in high (angstrom scale) resolution imaging applications. Therefore, to enable the use of standard, model-identification techniques, the image-based approach estimates the achieved position trajectory x from the acquired STM image.

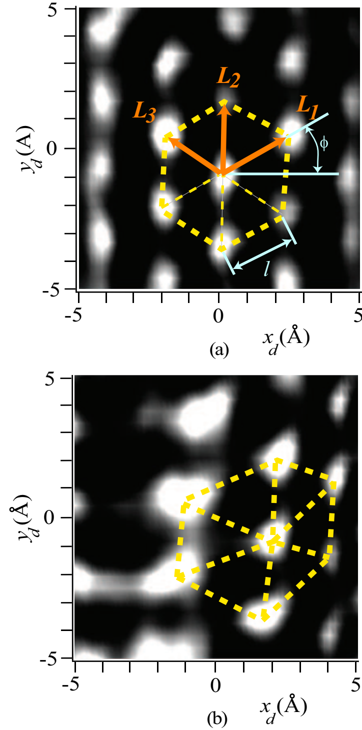

Fig. 2. Images using experimental data from STM. (a) A 1nm x 1nm image of a highly oriented pyrolytic graphite (HOPG) surface, which shows a hexagonal lattice structure that can be described by the lattice vectors L_1, L_2, and L_3 and the sample orientation ϕ. (b) SPM-probe positioning error (at high scan frequency) distorts the hexagonal lattice structure.

2) Data points on position trajectory from image: To determine data points on the SPM-position trajectory x from an image I, points of interest (POI) in the image I are compared with POI in a statically-calibrated, reference image I_{ref} acquired at low scan frequency., e.g., see Fig. 2(a). Such POI can include centers of carbon atoms in highly oriented pyrolytic graphite (HOPG) samples.

To illustrate this approach, consider the example in Fig. 3. A POI P from the image I (Fig. 3(b)) is acquired at time t_i. The image I can be compared to the reference image I_{ref} (Fig. 3(a)) to find the corresponding POI P_{ref} in the reference image I_{ref} — P and P_{ref} are the same point on the sample surface, they just appear at different locations in the two images due to positioning errors. Since the POI position does not change with the operating speed of the SPM, the location of the reference image POI P_{ref} can be used to infer the position of the POI P acquired at time t_i, yielding a data point $\{t_i, x(t_i)\}$ on the position trajectory $x(t)$ as shown in Fig. 3(c). Similarly, other POI in the image can be used to obtain a set of data points

$$\mathcal{X} = \{t_i, x(t_i)\}_{i=1}^{N_i} \tag{2}$$

on the position trajectory $x(t)$. Implementation details, such as image-processing to find the POI and mapping of the POI to the reference image, are discussed in [5], [6].

3) Periodic trajectories: If the the same probe-position trajectory is followed for each scan line, then the position

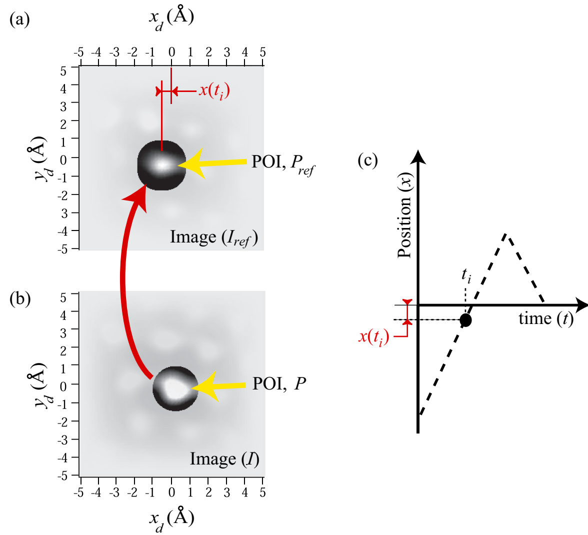

Fig. 3. Obtaining a data point $\{t_i, x(t_i)\}$ on the position trajectory $x(t)$ by comparing a high-frequency-scan image I with the reference image I_{ref}. (a) Low scan-frequency reference image. (b) High scan-frequency image. (c) Data point on high scan-frequency trajectory.

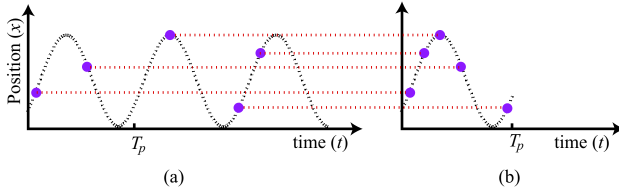

Fig. 4. Periodic trajectory case. (a) Data points in a periodic position trajectory $x(t)$. (b) data points mapped to a single time period $\mathcal{T} = [0, T_p)$ of the position trajectory.

trajectory $x(t)$ is periodic with time period T_p as shown in Fig. 4(a). Therefore, the position trajectory $x(t)$ only needs to be evaluated over the time interval $\mathcal{T} = [0, T_p)$ — see Fig. 4(b). The data points at time instants t_k outside this time interval $\mathcal{T}$ can be mapped into time points $\hat{t}_k$ in the time interval $\mathcal{T}$ where

$$t_k = \hat{t}_k + N_k T_p \quad (3)$$

for some integer N_k. These new data points $\{\hat{t}_k, x(t_k)\}$ are included in the set of data points $\mathcal{X}$ used to determine the position trajectory $x(t)$ with time t in the interval $\mathcal{T} = [0, T_p)$ as shown in Fig. 4(b).

C. Reconstruction of position $x(t)$ from data points $\mathcal{X}$

1) Reconstruction problem definition: For a position trajectory $x(t)$ that is band limited to f_{bw} Hz (i.e., frequency content is zero above f_{bw}) and a specific calibration sample (i.e., a defined POI pattern), the problem is to reconstruct the position trajectory $x(t)$ from the set of data points $\mathcal{X}$ obtained by using the image-based approach from section II-B.2.

2) Conditions for reconstruction: The position signal $x(t)$ can be reconstructed from a set of data points provided the image-based approach results in a sufficient number of well-

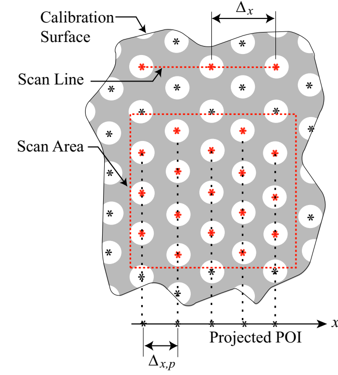

Fig. 5. Maximal spacing Δ_x between adjacent POI along scan path $x(t)$ and maximal spacing $\Delta_{x,p}$ between adjacent projected POI along the x axis.

spaced data points in the set $\mathcal{X}$, as shown in the following theorem.

Theorem: [Image-based reconstruction] The reconstruction problem ($\mathcal{X} \rightarrow x(t)$ in section II-C.1) can be solved if the minimal range $\underline{\delta}$ of the position trajectory over all time intervals of length $T_{ny}/2$ is greater than the maximal spacing Δ_x between adjacent POI along the scan trajectory $x(t)$ (illustrated in Fig. 5), i.e.,

$$\underline{\delta} > \Delta_x \quad (4)$$

where T_{ny} is the Nyquist period, $T_{ny} = 1/(2f_{bw})$.

Proof: If the data points in $\mathcal{X}$ are uniformly spaced in time, then the position trajectory $x(t)$ can be reconstructed, provided the sampling period T_u is less than the Nyquist period T_{ny} by Shannon's theorem, e.g. [17]. In general, the image-based method data points $\mathcal{X}$ are not uniformly spaced. However, a data point is always present within a quarter of the Nyquist period T_{ny} from any sequence of time instants t_k that are uniformly spaced at time interval T_u. This is because the range of the position trajectory $x(t)$ in the time interval $[t_k - T_{ny}/4, t_k + T_{ny}/4)$ (of length $T_{ny}/2$) is greater than the distance between the POI along $x(t)$ according to the theorem's condition (see equation 4). The presence of a data point within a quarter of the Nyquist period T_{ny} from the uniformly spaced time instants t_k satisfies the small-deviation-from-uniform-sampling condition (data samples less than $\frac{T_u}{4}$ away) for stable reconstruction from nonuniform samples according to the Paley, Wiener, and Levinson theorem, e.g., [18].

Corollary: [Reconstruction for periodic trajectories] When the position trajectory is periodic (with period T_p), let the POI in the scan area be projected onto the x axis and then let the maximal spacing between adjacent projected POI along the x axis be $\Delta_{x,p}$ as shown in Fig. 5. Then, the reconstruction result in the above theorem follows provided

$$\underline{\delta} > \Delta_{x,p}. \quad (5)$$

III. Application to STM

The implications of the reconstruction condition (Eq. 5) on the modeling of the nanopositioner dynamics in a scanning tunneling microscope (STM) are discussed in this section using images of a standard, highly-oriented-pyrolytic-graphite (HOPG), calibration sample, followed by experimental results.

A. Calibration sample properties

1) POI locations on calibration samples: Typical SPM calibration surfaces have spatially periodic features which can be used as POI. The feature locations can be described using 2-dimensional lattice vectors,

$$L = \{L_1, L_2, \ldots, L_n\}, \tag{6}$$

where $L_i \in \Re^2$. Using these lattice vectors, all feature locations can be determined as

$$p_{i_1,i_2,\ldots,i_n} = (x_0, y_0) + i_1 L_1 + i_2 L_2 + \cdots + i_n L_n, \tag{7}$$

where (x_0, y_0) is an initial feature location in the image and $i_1, i_2, \ldots, i_n$ are integers.

For example, HOPG samples have hexagonal lattice structures as shown in Fig. 2(a), which can be represented with three lattice vectors given by

$$\begin{aligned} L_1 &= (x_1, y_1) = (l\cos(\phi), l\sin(\phi)) \\ L_2 &= (x_2, y_2) = (l\cos(\phi+\pi/3), l\sin(\phi+\pi/3)) \\ L_3 &= (x_3, y_3) = (l\cos(\phi+2\pi/3), l\sin(\phi+2\pi/3)) \end{aligned} \tag{8}$$

where $l = 2.46\mathring{A}$ is the lattice spacing and ϕ is the sample orientation measured from the positive x axis.

2) Worst-case sample orientation: The sample orientation ϕ affects the maximal spacing $\Delta_{x,p}$ between adjacent projected POI along the x axis. Without loss of generality, it is assumed that a POI is at the origin, i.e. $(x_0, y_0) = (0, 0)$, and that the orientation is the rotation of the sample about the origin. Then, over all orientations ϕ, the worst-case, maximal distance between adjacent projected POI

$$\overline{\Delta}_{x,p} = \max_{\phi} \Delta_{x,p}, \tag{9}$$

occurs when the orientation is $\phi = \pi/6$ and is given by

$$\overline{\Delta}_{x,p} = l\cos(\pi/6) = \frac{\sqrt{3}}{2} l = 2.13\mathring{A}. \tag{10}$$

At this worst-case orientation, many POI project on the same point on the x axis as shown in Fig. 6(a).

3) Optimizing surface orientation: For the maximal distance between projected POI $\Delta_{x,p}$ to be small, the number of POI should be large and, ideally, be equally spaced in the x-direction. For example, deviations in orientation from the worst-case $\phi = \pi/6$ case result in POI projecting onto different points on the x axis, and thereby, resulting in a smaller maximal distance $\Delta_{x,p}$ between projected POI as shown in Fig. 6(b). Assuming that the POI will not leave the scan area, the deviation Ψ in the orientation from the worst-case orientation ($\phi = \pi/6$) can be found by requiring that the projected POI are equally spaced along the x axis.

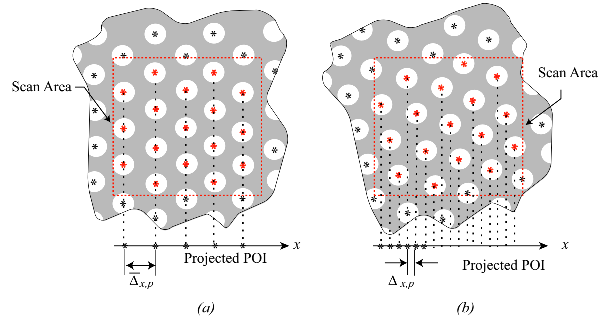

Fig. 6. Calibration sample orientation. (a) Orientation $\phi = \pi/6$, which corresponds to the maximal distance $\overline{\Delta}_{x,p}$ between adjacent projected POI over all orientations ϕ. Note that many POI project on the same point on the x axis. (b) Deviations from this $\phi = \pi/6$ orientation result in POI projecting onto different points on the x axis resulting in a smaller maximal distance $\Delta_{x,p}$ between projected POI.

For example, let the scan amplitude be an integer N_s multiple of the lattice vector l. Thus, there are N_s POI above and below the central POI included in the scan area as shown in Fig. 7(a). With a change in orientation of Ψ, the projected spacing between the central POI and the POI that was directly above it (when $\Psi = 0$) becomes $l\sin(\Psi)$ as shown in Fig. 7(b). This is true for any two, vertically adjacent, POI in any column of Fig. 7(a). To enable equal spacing between the projected POI, the projection of the top-most POI above the central POI must be separated from the projection of the bottom-most POI on the column to the left by $l\sin(\Psi)$, i.e.,

$$\begin{aligned} N_s l\sin(\Psi) &+ \left(N_s - \frac{1}{2}\right) l\sin(\Psi) \\ &+ l[1-\cos(\Psi)]\cos(\pi/6) \\ &+ l\sin(\Psi) = l\cos(\pi/6). \end{aligned} \tag{11}$$

Therefore, the optimal deviation Ψ^* (from orientation $\phi = \pi/6$) for the smallest maximal distance between projected POI is

$$\Psi^* = \tan^{-1}\left(\frac{\sqrt{3}}{4N_s+1}\right). \tag{12}$$

The corresponding smallest maximal distance between projected POI is

$$\underline{\Delta}_{x,p} = l\sin(\Psi^*) = l\sin\left[\tan^{-1}\left(\frac{\sqrt{3}}{4N_s+1}\right)\right] \tag{13}$$

For $N_s = 2$ (scan amplitude of approximately 5Å) the optimal deviation from $\phi = \pi/6$ is $\Psi = 0.190 rads$, or a total sample rotation of $\phi = 0.714 rads$. This corresponds to a smallest maximum distance $\underline{\Delta}_{x,p} = 0.465$Å.

4) Variation of maximal spacing with orientation: The variation of the maximum projected POI spacing ($\Delta_{x,p}$) with orientation is illustrated in Fig. 8. For this example, the maximum projected POI spacing ($\Delta_{x,p}$) is plotted with respect to surface orientation (ϕ) from 0 to 60 degrees for a 1nm x 1nm scan area and a lattice spacing of $l = 2.46$Å (HOPG). From Fig. 8, the worst case maximal distance is

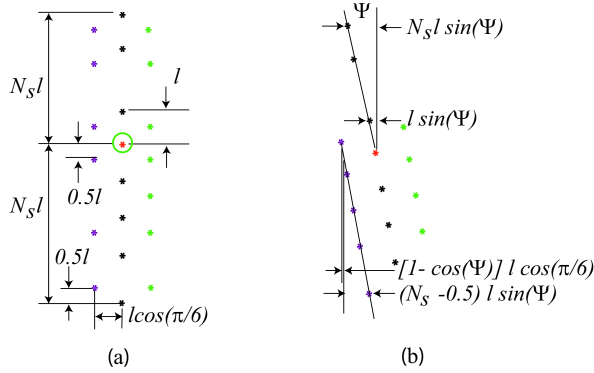

Fig. 7. (a) Worst-case orientation $\phi = \pi/6$. (b) Deviation Ψ from the orientation $\phi = \pi/6$. l is the lattice spacing.

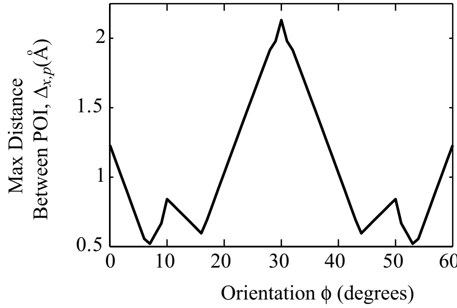

Fig. 8. Simulation results for maximum distance between adjacent POI ($\Delta_{x,p}$) as a function of rotation (ϕ).

$\bar{\Delta}_{x,p} = 2.13$Å and occurs at $\phi = 30^o = \pi/6$, as calculated in Eq. 10. The calculated smallest maximal distance $\underline{\Delta}_{x,p}$ is not captured in this plot, due to POI leaving the scan area. The trends related to the smallest maximal distance are, however, captured. Starting from $\phi = 30$, as the sample is rotated (Ψ), the maximal distance decreases because the POI column endpoints get closer, eventually reaching a minimum.

B. Sinusoidal position trajectory

The effects of position trajectory properties (frequency and amplitude) on the minimal range $\underline{\delta}$ of the position trajectory (see Eq. 5) over all time intervals of half the Nyquist length $T_{ny}/2$ are investigated below.

1) Frequency of position trajectory: Consider a sinusoidal position trajectory of frequency ω $rads/s$ and amplitude A_x

$$x(t) = A_x \sin(\omega t) \tag{14}$$

as shown in Fig. 9. Then, the time period is $T_p = 2\pi/\omega$, the Nyquist period is $T_{ny} = T_p/2$, and the minimal range $\underline{\delta}$ is to be found over all time intervals of half the Nyquist length $T_{ny}/2 = T_p/4$. This minimum range $\underline{\delta}$ occurs when the time interval of length $T_p/4$ is centered around the turning points of the sinusoid, e.g., at $T_p/4$ or $3T_p/4$ and is given by

$$\begin{aligned} \underline{\delta} &= A_x \left\{\sin[\omega T_p/4] - \sin[\omega(T_p/4 - T_p/8)]\right\} \\ &= A_x \left(1 - \sin(\pi/4)\right) \quad = A_x(1 - 1/\sqrt{2}) \end{aligned} \tag{15}$$

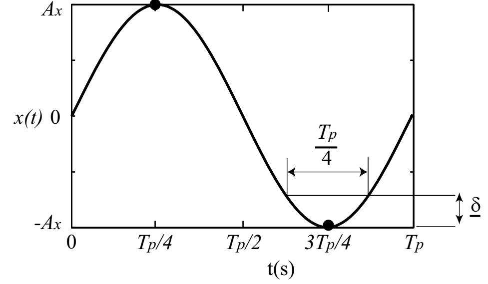

Fig. 9. Illustration for calculating the minimum range for a sinusoidal trajectory in Eq. 14.

Thus, for a single frequency sinusoidal position trajectory, the minimum range $\underline{\delta}$, that affects the reconstruction condition (Eq. 5), is independent of the frequency.

2) Amplitude of position trajectory: The scan amplitude A_x of the position trajectory can be chosen to increase the minimum range $\underline{\delta}$ (in Eq. 15) of the sinusoidal position trajectory. Therefore, the amplitude can be chosen to satisfy the reconstruction condition in Eq. 5. For example, a large enough scan amplitude will ensure satisfying the reconstruction condition over all orientations ϕ of the calibration sample, i.e., (from Eqs. 5, 9)

$$\underline{\delta} > \overline{\Delta}_{x,p} > \Delta_{x,p} \tag{16}$$

which is satisfied provided, from Eqs. 9 and 15,

$$A_x(1 - 1/\sqrt{2}) > \frac{\sqrt{3}}{2} l \quad \Longrightarrow \quad A_x \; > l\frac{\sqrt{3}}{(2-\sqrt{2})} = \underline{A_x}. \tag{17}$$

For the HOPG sample ($l = 2.46\mathring{A}$), a scan amplitude greater than the minimum scan amplitude of $\underline{A_x} = 2.95l = 7.27\mathring{A}$ will ensure that the sinusoidal output position can be reconstructed for any orientation of the HOPG sample.

C. Experimental results

Experimental STM images of HOPG were used to identify the model of the nanopositioner in a Burleigh Metris-1000 Scanning Tunneling Microscope.

1) Experimental setup: Images with a desired scan area of $1nm$ x $1nm$ were acquired (with 50 by 50 pixel resolution) in constant height mode using a hand-cut PtIr (80/20) tip. The images were obtained using a sinusoidal trajectory to enable STM modeling (see section II-B1). The POI in the images were chosen as the centers of the carbon atoms and the POI in the image I and the reference image I_{ref} were mapped (i.e. the same points on the sample surface were found – see section II-B2) based on proximity [5].

2) Calibration sample and position trajectory for given scan area: The HOPG sample rotation angle was chosen to be $\phi = \pi/4$, which corresponds to a maximal distance between projected POI of $\Delta_{x,p} \approx 0.64$Å from Fig. 8. Given this maximum distance Δ_x, the minimum sinusoidal scan amplitude can be found (similar to Eq. 17).

$$A_x(1 - 1/\sqrt{2}) > \Delta_{x,p} \quad \Longrightarrow \quad \underline{A_x} \; = \frac{\Delta_{x,p}}{1 - 1/\sqrt{2}}, \tag{18}$$

yielding, when $\Delta_{x,p} \approx 0.64$Å, a minimum scan amplitude of $\underline{A_x} = 2.18$Å. Thus, the sinusoidal x-trajectory magnitude $A_x = 5$Å that is greater than 2.18Å is acceptable.

3) Swept Sine Modeling: A model of the STM system can be identified using the swept sine modeling technique. At any scan frequency (ω), the transfer function $\hat{G}(s)|_{s=\mathbf{i}\omega}$, $\mathbf{i} = \sqrt{-1}$, can be found if the response of the system to a sinusoidal input can be measured. In particular, let a sinusoidal input, $u = M_u \sin(\omega t + \phi_u)$, where M_u and ϕ_u are the magnitude and phase of the input, result in a sinusoidal output of the same frequency (after transients have died out), $x = M_x \sin(\omega t + \phi_x)$, where M_x and ϕ_x are the magnitude and phase of the output. The magnitudes and phases of the input (u) and output (x) can be compared to determine the magnification, $M_\omega = |\hat{G}(s)|_{s=\mathbf{i}\omega} = M_x/M_u$ and phase shift, $\theta_\omega = [\angle\hat{G}(s)]_{s=\mathbf{i}\omega} = \phi_x - \phi_u$, of the dynamic response at the given frequency (ω) [19].

The output (x) for a known input (u) can be measured using the image-based method for a range of frequencies from $\vec{\omega}$, yielding magnification $\vec{M_\omega}$ and phase shift $\vec{\theta_\omega}$ vectors. From the magnification and phase shift information, a transfer function model of the dynamics can be found a using least-squares curve fitting algorithms such as the MATLAB function $invfreqs()$.

Following this method, the STM model was found up to $2KHz$, in Ref. [6], as

$$\hat{G}(s) = \frac{3.71 \times 10^4(s^2 - 3.23 \times 10^4 s + 2.68 \times 10^8}{(s + 3278)(s^2 + 1840s + 3.87 \times 10^8)}. \quad (19)$$

A frequency response plot of this model can be seen in FIG. 10.

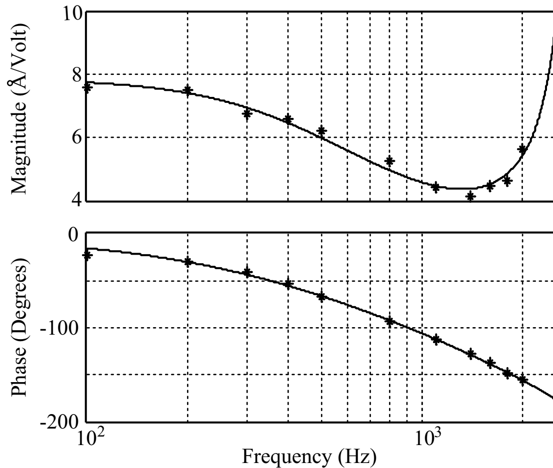

Fig. 10. Frequency response obtained using the image based method [6]. The points obtained using the method are show as asterisks (*) and the model is shown as a solid line.

IV. CONCLUSIONS

The article developed conditions on the calibration sample that allow for the image-based identification of SPM-nanopositioner dynamics. In particular, relations were developed between: (a) the minimum spacing between features and the orientation of the calibration sample, and (b) the amplitude and frequency content of the SPM-probe's position trajectory. These conditions were applied to identify a dynamics model of a STM using images of a HOPG sample.

ACKNOWLEDGMENT

This work was supported by NSF Grant CMS 0301787

REFERENCES

[1] S. Devasia, E. Eleftheriou, and S. O. R. Moheimani, "A survey of control issues in nanopositioning," *IEEE Transactions on Control Systems Technology*, vol. 15(5), pp. 802–823, Sept, 2007.

[2] D. Alliata, C. Cecconi, and C. Nicolini, "A simple method for preparing calibration standard for the three working axes of scanning probe microscope piezo scanners," *Review of Scientific Instruments*, vol. 67(3), pp. 748–751, 1996.

[3] H. Edwards, J. F. Jorgensen, and J. Dagata, "Influence of data analysis and other factors on the short-term stability of vertical scanning-probe microscope calibration measurements," *J. Vac. Sci. Technol. B*, vol. 16, pp. 633–644, 1998.

[4] R. V. Lapshin, "Automatic drift elimination in probe microscope images based on techniques of counter-scanning and topography feature recognition," *Measurement Science and Technology*, vol. 18, no. 3, pp. 907–27, February 2007.

[5] G. M. Clayton and S. Devasia, "Image-based compensation of dynamic effects in scanning tunneling microscopes," *Nanotechnology*, vol. 16, no. 6, pp. 809–18, June 2005.

[6] ——, "Iterative image-based modeling and control for higher scanning probe microscope performance," *Review of Scientific Instruments*, vol. 78, no. 8, p. 083704, August 2007.

[7] K. Wilder, H. T. Soh, A. Atalar, and C. F. Quate, "Nanometer-scale patterning and individual current controlled lithography using multiple scanning probes," *Review of Scientific Instruments*, vol. 70, no. 6, pp. 2822–2827, June 1999.

[8] M. Zhang, D. Bullen, S.-W. Chung, S. Hong, K. S. Ryu, Z. Fan, and C. A. Mirkin, "A MEMS nanoplotter with high-density parallel dip-pen nanolithography probe arrays," *Nanotechnology*, vol. 13, no. 2, pp. 212–17, April 2002.

[9] E. Eleftheriou, T. Antonakopoulos, G. K. Binnig, G. Cherubini, M. Despont, A. Dholakia, U. Durig, M. A. Lantz, H. Pozidis, H. E. Rothuizen, and P. Vettiger, "Millipede a MEMS-based scanning-probe data-storage system," *IEEE Transactions on Magnetics*, vol. 39, no. 2, pp. 938–45, March 2003.

[10] L. Aeschimann, A. Meister, T. Akiyama, B. W. Chui, P. Niedermann, H. Heinzelmann, N. F. DeRooij, U. Staufer, and P. Vettiger, "Scanning probe arrays for life sciences and nanobiology applications," *Microelectronic Engineering*, vol. 83, no. 4-9, pp. 1698–1701, April-September 2006.

[11] S. Tien, Q. Zou, and S. Devasia, "Iterative control of dynamics-coupling-caused errors in piezoscanners during high-speed AFM operation," *IEEE Transactions on Controls Systems Technology*, vol. 13, no. 6, pp. 921–31, November 2005.

[12] R. Paley and N. Wiener, *Fourier Transforms in the Complex Domain*. American Mathematics Society, 1934.

[13] N. Levinson, *Gap and Density Theorems*. American Mathematics Society, 1940.

[14] W. A. Hofer, A. S. Foster, and A. L. Shluger, "Theories of scanning probe microscopes at the atomic level," *Reviews of Modern Physics*, vol. 75, no. 4, pp. 1287–331, October 2003.

[15] D. Croft and S. Devasia, "Vibration compensation for high speed scanning tunneling microscopy," *Review of Scientific Instruments*, vol. 70, no. 12, pp. 4600–5, December 1999.

[16] D. Croft, G. Shedd, and S. Devasia, "Creep, hysteresis, and vibration compensation for piezoactuators: Atomic force microscopy application," *ASME Journal of Dynamic Systems, Measurement and Control*, vol. 123(35), pp. 35–43, March, 2001.

[17] C. E. Shannon, "Communications in the presence of noise," *Proceedings of the IRE*, vol. 137, no. 1, pp. 10–21, January 1949.

[18] K. Yao and J. B. Thomas, "On some stability and interpolatory properties of nonuniform sampling expansions," *IEEE Transactions on Circuit Theory*, vol. CT-14, no. 4, pp. 404–8, December 1967.

[19] D. Rowell and D. Wormley, *System Dynamics: An Introduction*. Prentice Hall, 1997.